

## Research



**Cite this article:** Klima RL, Petro NE. 2017  
Remotely distinguishing and mapping  
endogenic water on the Moon. *Phil. Trans. R.  
Soc. A* **375**: 20150391.  
<http://dx.doi.org/10.1098/rsta.2015.0391>

Accepted: 14 December 2016

One contribution of 9 to a Theo Murphy  
meeting issue ‘The origin, history and role of  
water in the evolution of the inner Solar  
System’.

### Subject Areas:

Solar System, space exploration,  
spectroscopy, geology

### Keywords:

Moon, water, hydroxyl, infrared spectroscopy,  
remote sensing

### Author for correspondence:

Rachel L. Klima  
e-mail: [rachel.klima@jhuapl.edu](mailto:rachel.klima@jhuapl.edu)

Electronic supplementary material is available  
online at [https://dx.doi.org/10.6084/m9.  
figshare.c.3700012](https://dx.doi.org/10.6084/m9.figshare.c.3700012).

# Remotely distinguishing and mapping endogenic water on the Moon

Rachel L. Klima<sup>1</sup> and Noah E. Petro<sup>2</sup>

<sup>1</sup>Space Exploration Sector, Planetary Exploration Group, Johns  
Hopkins University Applied Physics Laboratory, 11100 Johns Hopkins  
Road, Laurel, MD 20723, USA

<sup>2</sup>NASA Goddard Space Flight Center, Greenbelt, MD, USA

RLK, 0000-0002-9151-6429

Water and/or hydroxyl detected remotely on the lunar surface originates from several sources: (i) comets and other exogenous debris; (ii) solar-wind implantation; (iii) the lunar interior. While each of these sources is interesting in its own right, distinguishing among them is critical for testing hypotheses for the origin and evolution of the Moon and our Solar System. Existing spacecraft observations are not of high enough spectral resolution to uniquely characterize the bonding energies of the hydroxyl molecules that have been detected. Nevertheless, the spatial distribution and associations of H, OH<sup>-</sup> or H<sub>2</sub>O with specific lunar lithologies provide some insight into the origin of lunar hydrous materials. The global distribution of OH<sup>-</sup>/H<sub>2</sub>O as detected using infrared spectroscopic measurements from orbit is here examined, with particular focus on regional geological features that exhibit OH<sup>-</sup>/H<sub>2</sub>O absorption band strengths that differ from their immediate surroundings.

This article is part of the themed issue ‘The origin, history and role of water in the evolution of the inner Solar System’.

## 1. Introduction

The Moon is a unique laboratory for understanding the evolution of solid planets in the Solar System. As the only extra-terrestrial body for which we have both orbital data and samples collected from known locations on the surface, it offers an opportunity to link global-scale processes with high-precision laboratory analyses. The lunar magma ocean (LMO) hypothesis [1,2] has become

the paradigm for the formation of terrestrial planets, as well as some of the larger asteroids. In a magma ocean, the heat of accretion and radioactive decay leads to a convecting, molten magma layer, from which minerals gradually crystallize. In the case of the LMO, the earliest crystallizing mineral would have been magnesium-rich olivine, followed by orthopyroxene, both of which would have settled to the bottom of the magma ocean. The ocean would have gradually increased in iron and aluminium content, as aluminium is not preferred by either olivine or orthopyroxene and in both minerals magnesium is more compatible than iron. As magnesium became scarcer, the iron content and density of the crystallizing minerals would have increased. Eventually, the residual liquid would have become enriched enough in aluminium to crystallize plagioclase feldspar. Plagioclase, being less dense than the iron-rich liquid, would have floated to the surface to form the lunar crust. Ultimately, sandwiched between the lower cumulate pile and the crust, there would have been a dense liquid, enriched in iron, titanium, rare-earth elements, and any other elements that were highly incompatible with the three primary mineral groups, olivine, pyroxene, and plagioclase. A record of these last dregs of the LMO can be found by measuring trace elements to search for the distinctive geochemical component known as 'KREEP' due to its enhancement in potassium (K), rare-earth elements (REE) and phosphate (P). The cumulate pile beneath the crust, capped by these incompatible element-rich liquids (urKREEP), would have been least dense at the bottom and most dense at the top, resulting in gravitational instability, which led to convective overturn of the lunar mantle and magmatism [3].

Despite decades during which the Moon was interpreted as being highly depleted in water and other volatile elements, reanalysis with modern instruments of the lunar samples now suggests that some water persists in the lunar interior. The lunar samples lack typical hydrous mineral phases such as amphibole; however, studies of lunar pyroclastic glasses [4,5] and apatite crystals (e.g. [6–8]) in the last decade suggest that water is present in at least some lunar interior reservoirs, perhaps at concentrations similar to terrestrial mid-ocean-ridge basalts (MORBs) (i.e. [9–11]). The pyroclastic glasses, which represent the most primitive liquids among the current lunar samples, provide a relatively straightforward record of volatiles in the source region. Nanoscale secondary ion mass spectrometry measurements across individual pyroclastic beads reveal that volatile elements are not only present, but that their concentration decreases from the cores of the beads towards the edges, consistent with magmatic degassing on ascent [4,5]. Models of the degassing profiles imply that the source region of the pyroclastic glasses contained at least 260 ppm H<sub>2</sub>O, with around 760 ppm being more likely. Abundances of OH<sup>−</sup> measured in apatite, a late-stage mineral present in many lunar rock types, are more difficult to quantitatively extrapolate to their source concentrations due to the uncertainties in partitioning behaviour of volatiles between apatite and liquids of different composition. Apatites have been found to contain a range of OH<sup>−</sup> concentrations, with the highest being found in the mare basalts and the lowest values typically found in KREEP-rich intrusive samples. This distribution of OH<sup>−</sup> in the lunar rocks is somewhat counterintuitive. One might expect that water, which is incompatible with the nominally anhydrous minerals that dominate the LMO cumulates, should have been concentrated in urKREEP. However, analyses of existing lunar samples, including Mg- and alkali-suite rocks and KREEP-rich basalts, typically contain the driest of the lunar apatites, suggesting that OH<sup>−</sup> is decoupled from KREEP in the lunar interior (e.g. [9–13]).

Evidence from orbit has also revealed hydroxyl and potentially water distributed across the entire lunar surface. The Moon Mineralogy Mapper (M<sup>3</sup>) was a near-infrared imaging spectrometer that measured reflected sunlight to map lunar mineralogy, flown on India's Chandrayaan-1 spacecraft [14]. Although water was not expected over the majority of the Moon, M<sup>3</sup>'s wavelength range was extended to 3000 nm in order to enable detection of any water on the surface of a few polar craters. Despite expectations, M<sup>3</sup> detected a broadly distributed OH<sup>−</sup> signature present across the lunar surface, with abundances increasing towards the poles [15]. This observation was confirmed by independent analyses of EPOXI [16] and Cassini [17] near-infrared data that extended beyond 3000 nm, but at lower spatial resolution. The spatial distribution, coupled with evidence that the OH<sup>−</sup> absorption band strength varied as a function of the time of lunar day, led to the conclusion that a majority of this OH<sup>−</sup> had been produced *in situ*

by the solar-wind hydrogen interacting with oxygen in minerals in the lunar regolith [15,16,18]. It was also recognized that some portion of the  $\text{OH}^-$  signature could be intrinsic to the Moon or deposited by cometary impacts [15,17].

Distinguishing endogenic water and mapping its distribution would provide valuable global-scale constraints to complement lunar sample studies, particularly when trying to understand the relationship between  $\text{OH}^-$  and KREEP. All lunar samples returned by robotic or human missions were collected on the lunar nearside, with most of them collected within or near the Procellarum KREEP Terrane (PKT), a region that encompasses many of the lunar maria that was observed by the gamma-ray spectrometer on the Lunar Prospector mission to contain high amounts of thorium [19]. Although billions of years of mixing through impacts has resulted in a broad array of lithologies being present at any collection site, there is still undoubtedly bias in the returned samples towards representing a limited sampling area (approx. 4% of the lunar surface) [20]. Lunar meteorites provide additional data for regions that may reside anywhere on the Moon, but the specific provenance of each meteorite is unknown. The overprinting of solar wind-produced  $\text{OH}^-$  complicates the assessment of the distribution of endogenic  $\text{OH}^-$  from orbit. We here examine spectral data of specific locations that might be expected, based on morphology or composition, to exhibit endogenic  $\text{OH}^-$ . In addition, we examine maps of  $\text{OH}^-$  absorption band strength to search for localized positive anomalies that might be attributed to endogenic  $\text{OH}^-$ . These data are then compared with Lunar Prospector thorium maps [21] to determine whether, at least to first order, localized  $\text{OH}^-$  anomalies are directly correlated with KREEP content.

## 2. Material and methods

This study centres on data from the  $\text{M}^3$ . The  $\text{M}^3$  was designed to operate in two sampling modes, global and targeted. Full spatial resolution (600 cross-track pixels at 70 m per pixel) and full spectral resolution (260 bands at 10 nm from approximately 400–3000 nm) targeted data were obtained for only a limited number of locations on the Moon, largely because of the early end of the mission. However, almost the entire lunar surface was imaged at the reduced-resolution global mode (140 m per pixel from a 100 km orbit, 280 km per pixel from a 200 km orbit and 85 spectral bands) [22,23]. The  $\text{M}^3$  data are calibrated using a combination of pre-flight and in-flight calibration procedures [22], and have been registered by ray-tracing each  $\text{M}^3$  spatial element on the lunar surface to an initial Lunar Orbiter Laser Altimeter-derived lunar reference frame [23]. Level 2 data, used in this analysis, have had thermal emission at long wavelengths empirically removed [24] and have been photometrically corrected to a viewing geometry of  $30^\circ$  incidence and  $0^\circ$  emission [25]. These data are publicly available in the NASA Planetary Data System (PDS; <http://pds-imaging.jpl.nasa.gov/volumes/m3.html>). We incorporate data collected during optical periods 1b, 2a and 2c1. Data from optical periods 1b and 2a are used whenever available for local-scale investigations, as those data were collected while Chandrayaan-1 was still in a 100 km orbit and therefore are at a higher spatial resolution (approx. 140 m per pixel) than are data from optical period 2c1 (approx. 280 m per pixel) [23]. These data were obtained during the lunar morning and afternoon, and generally exhibit more directly comparable temperatures than do those collected closer to lunar noon (OP2c1).

Water and hydroxyl can be identified in near-infrared data near 3000 nm, the energy at which the O–H fundamental stretching mode produces a strong absorption band that can be used to identify  $\text{OH}^-$  at levels as small as a few ppm. Transmission measurements of glasses and minerals using Fourier-transformed infrared spectroscopy are commonly used to quantify water in both hydrated and nominally anhydrous phases (e.g. [26]). However, quantification of water content from near-infrared reflectance data is complicated by a number of factors. Transmission microscopy minimizes scattering of light off the surface of the sample and primarily measures the absorbance within the body of the mineral, allowing Beer's law to be applied with only a straightforward correction for the mineral absorption properties. Reflectance measurements in the near-infrared rely on light scattering off grain interfaces, through mineral grains, and ultimately

back towards the sensor. In remotely sensed measurements, the scattering regime is very poorly constrained, as particle size, porosity and the physical distribution of the  $\text{OH}^-$  molecules (e.g. randomly filling defects and vacancies within the mineral structure or adsorbed between mineral grains) are normally unknown. Using assumptions for the regolith properties, radiative transfer modelling can be used to estimate the path length of light, and then Beer's law can be applied to determine the concentration. Each assumption adds additional uncertainty, and errors may be very poorly constrained. Milliken & Mustard [27–29] examined adsorption of per cent levels of  $\text{H}_2\text{O}$  and  $\text{OH}^-$  on Mars-relevant minerals using reflectance spectroscopy in the laboratory to evaluate which, if any, parameters best predicted the water content. They concluded that the effective single-particle absorption thickness (ESPAT) parameter as defined by Hapke [30] could be used to estimate water abundances from absorption band strength. Li & Milliken [31] have extended these studies to focus on more lunar-relevant materials and lower water contents. Using these or any other methods, quantitative estimates of abundance still rely directly on assumptions made about the grain size of the particles that either contain or are coated by  $\text{OH}^-$ .

In the case of the Moon, thermal emission of the lunar regolith further complicates characterization of  $\text{H}_2\text{O}$  and  $\text{OH}^-$ . The higher the temperature of the surface, the more the short-wavelength tail of the thermal black-body emission curve distorts the apparent strength of any absorption band near 3000 nm. The equatorial temperature of the surface of the Moon varies by approximately 300°C over the course of a lunar day [32], and depends on a wide range of factors including solar illumination, time of day, albedo, rock abundance, soil particle size distribution, bulk density, thermal conductivity and heat capacity. Although the  $\text{M}^3$  data delivered to the PDS used an empirical thermal correction to remove a first-order thermal component from the warmest surfaces [24], other methods for removing the thermal component from the  $\text{M}^3$  spectra are being explored, including using relationships from laboratory measurements of lunar materials [31] and using radiative modelling and a roughness model to account for anisothermality [33]. Because those data are not currently publicly available, we rely on the PDS-archived level 2 products and instead work to minimize the uncertainties introduced by differences in the thermal components of each spectrum by comparing each location of interest with others of similar lithology and albedo measured at the nearest possible time of lunar day and latitude.

The relative strength of the  $\text{OH}^-$  absorption band near 2800 nm is parametrized here using the following equation:

$$\text{OH}^- \text{ relative band depth} = 1 - \frac{\text{BR}}{\text{sCR}}, \quad (2.1)$$

where short-wavelength continuum reflectance (sCR) is the average of the reflectance measured at 2616 nm and 2656 nm and band reflectance (BR) is the average of the reflectance measured at 2776 nm and 2816 nm. We refer to this quantity as 'relative band depth' rather than 'band depth' because the wavelength range of  $\text{M}^3$  is not sufficiently long to provide an anchor point outside of the  $\text{OH}^-$  absorption band on the long-wavelength side. Thus, the relative band depth is not solely influenced by  $\text{OH}^-$  band strength, but also by spectral slope, which may be caused by residual thermal component and/or maturity. We average two channels inside and outside of the  $\text{OH}^-$  band region to try to reduce the sensitivity of this parameter to noise in regions with low signal strength. Larger  $\text{OH}^-$  relative band depth values indicate the presence of a substantial 2800 nm band. However, because regions of the Moon that are space-weathered exhibit a strong red-sloping continuum, in some cases a band may still be present when the  $\text{OH}^-$  relative band depth value is near or even slightly below zero (electronic supplementary material, figure S1). Although the frequency of the O–H stretch near 3000 nm can, in principle, be used to distinguish between  $\text{OH}^-$  and  $\text{H}_2\text{O}$ , the exact band minimum observed in  $\text{M}^3$  data depends greatly on spectral resolution and the accuracy of the thermal correction of the data. We thus refer exclusively to  $\text{OH}^-$ , as it is the O–H stretch being mapped.

It is important to note that reflectance spectroscopy is sensitive only to the uppermost surface of the lunar regolith, generally a depth of tens to thousands of microns depending on the optical properties of the regolith. We compare our data with those collected by the Lunar

Prospector Gamma-Ray Spectrometer (LPGRS), which is sensitive to depths of tens of centimetres, but at several orders of magnitude coarser spatial resolution than measured by  $M^3$ . If any  $OH^-$  band detected is present only as a thin layer on the surface, or represents only a small fraction of an LPGRS pixel, any thorium detection could be derived from beneath or around the  $OH^-$ -enriched material.

### 3. Results

#### (a) Global distribution of hydroxyl

A global map of the  $OH^-$  relative band depth index and the relationship between measured  $OH^-$  relative band depth and reflectance at 750 nm are presented in figure 1. The strongest  $OH^-$  absorption features occur north and south of about  $60^\circ$  latitude (figure 1*b*; box 4), as noted previously [15–18]. In several locations, the boundary of this broadly distributed  $OH^-$  signature curves around major mafic terrains, such as the mafic anomaly in the South Pole–Aitken (SPA) Basin and Mare Frigoris, suggesting that, to first order,  $OH^-$  adsorbs more readily onto anorthosite than iron-bearing olivines and pyroxenes (figure 1*b*, box 1). This lithological preference was reported by Cheek *et al.* [34] for the north polar region, and is consistent with laboratory studies that show that plagioclase minerals can adsorb roughly twice as much  $OH^-$  or  $H_2O$  as basalts or glasses [35,36].

At lower latitudes, large-scale regional  $OH^-$  relative band depths are generally slightly negative, suggesting that any  $OH^-$  signatures present are swamped by the overall spectral slope of measurement (electronic supplementary material, figure S1). The  $OH^-$  relative band depths measured in the highlands are slightly stronger than in the mare, though data in both regions correlate with reflectance at 750 nm (figure 1*b*; boxes 1,2). The lower  $OH^-$  relative band depths in the maria than in the highlands may be due to adsorption properties of the minerals. However, they may also be in some part attributed to the overall low albedo of the warm maria, where thermal emission is high and often incompletely removed by the methods of Clark *et al.* [24].

Distinct from the mid-latitude highland trend (figure 1*b*; box 2) is a zone of figure 1*b* in which the correlation between  $OH^-$  relative band depth and albedo shallows and almost disappears (figure 1*b*; box 3, part of box 4). Although these data include high-latitude  $OH^-$ , they also include smaller, localized  $OH^-$  anomalies that are scattered throughout the lower latitudes. We focus our examination of local-scale features primarily on these  $OH^-$  relative band depth anomalies in brighter, non-mare, lithologies. We refer readers to the work of Li & Milliken [31,37,38] for an investigation of anomalies in darker terrains using a revised thermal correction.

The range and standard deviation in  $OH^-$  relative band depths as a function of latitude for the higher spatial resolution data (O1b and OP2a) are depicted in figure 2. When compared with the global latitudinal distribution presented in McCord *et al.* [18], the  $OH^-$  minimum in the data is slightly skewed towards the northern hemisphere. This is due to the higher relative concentration of maria, which exhibit overall lower  $OH^-$  relative band depths, in the northern hemisphere of the high-resolution dataset. Local-scale enhancements in excess of the regional mean occur across the Moon.  $OH^-$ -enhanced spots are generally associated with geological features of scales of tens of kilometres or less; however, these individual spots may be geologically associated with larger regional features, such as the rings of the Orientale or Imbrium Basins. Because of the small scale of most  $OH^-$  anomalies, we surveyed 56 locations of interest, drawn from the list of small-scale thorium anomalies in Lawrence *et al.* [21] and the orthopyroxene-rich deposits in Klima *et al.* [39] (electronic supplementary material, table S1), using the highest resolution  $M^3$  data available. The maximum  $OH^-$  relative band depth for each of these regions is overlain on the mean global relative band depth trend in figure 2. Enhanced  $OH^-$  relative band depths occur in all terrain groups: highlands, SPA and PKT. Hydroxyl signatures occur in association with olivine, orthopyroxene and anorthosite, as well as with silicic material. They are not exclusively associated with enhanced thorium levels, but are slightly more often associated with thorium highs than lows (figure 2; electronic supplementary material, table S1). Although



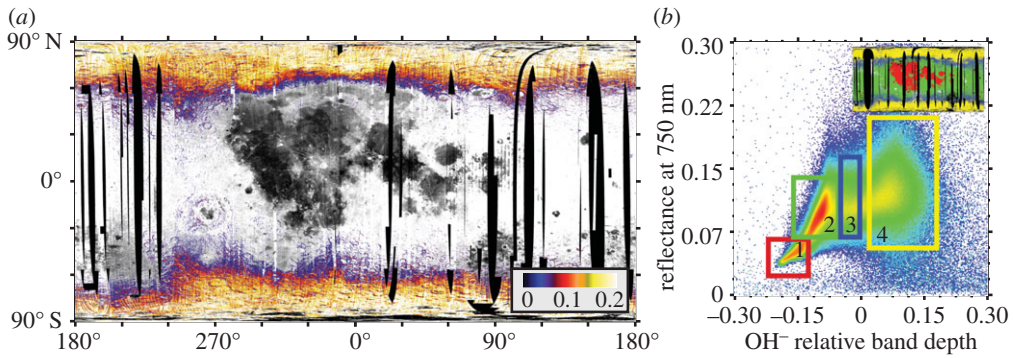


**Figure 1.** (a) Global distribution of  $\text{OH}^-$  relative band depth as measured by the  $\text{M}^3$  instrument. Data from optical periods 1b, 2a and 2c1 are included.  $\text{OH}^-$  relative band depth is depicted as a colour ramp overlain on a 750 nm reflectance basemap. Regions with near-zero relative band depths have been made transparent to show the relationship of absorption band strength to major terrains. Map projection is simple cylindrical. (b) Density plot of the global relationship between 750 nm reflectance and  $\text{OH}^-$  relative band depth. At least two trends can be discerned—the equatorial trend, which exhibits a roughly linear relationship between reflectance and relative band depth, ranging from the mare regions (box 1, red on inset map) to highland regions (box 2, green on inset map), and a high-latitude trend, primarily encompassing higher reflectance terrains. It is only at latitudes poleward of about approximately  $60^\circ$  that absorption relative band depths become consistently positive on a regional scale (box 4, yellow on inset map), although there are some small local anomalies showing positive  $\text{OH}^-$  relative band depths in both the mare and the highlands.

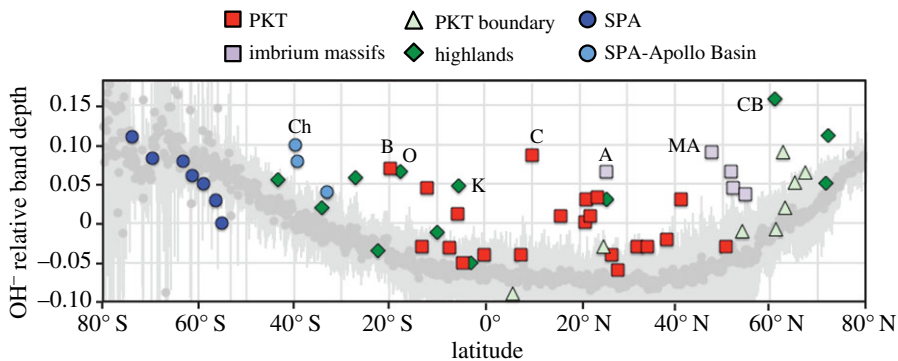


**Figure 2.** Global and localized  $\text{OH}^-$  relative band depths on the Moon as a function of latitude. Dark grey circles represent the mean  $\text{OH}^-$  relative band depths for 13 longitudinal transects distributed across the Moon and spaced approximately evenly throughout terrain measured during optical periods 1b and 2a, with the standard deviation shown in light grey. Overlain on these data are  $\text{OH}^-$  relative band depth values for 55 locations of interest, coloured based on the terrain they reside in. Eight of these locations that exhibit  $\text{OH}^-$  relative band depths more than twice the standard deviation are labelled: Ch, Chaffee S; B, Bullialdus; O, Mare Orientale; K, Korolev; C, Copernicus; A, Apennine Bench; MA, Montes Alpes; CB, Compton–Belkovich.

there is significant variability on a global scale, just over 15% of the locations examined exhibit  $\text{OH}^-$  relative band depths more than twice the standard deviation for their respective latitudes. Nine of these sites, spanning the full latitudinal range of the Moon, are labelled in figure 2 and described in more detail in table 1. In general, the strongest of these  $\text{OH}^-$  anomalies are associated with thorium enhancements; however, Copernicus is associated with a thorium low [20].

## (b) Geological context of local-scale hydroxyl enhancements

The most prominent local-scale  $\text{OH}^-$  enhancements revealed in this study (table 1) are associated with specific geological features, all of which represent deep crustal material exposed at the surface: silicic domes/constructs, basin rings, central peaks and massifs. Examples of the spectra

**Table 1.** Selected locations of enhanced OH<sup>−</sup>. An, anorthosite; OPX, orthopyroxene; Ol, olivine.

location	lon	lat	minerals	thorium	notes/geological association
Chaffee S	−157.5	−39.8	OPX	—	inner ring of Apollo Basin
Bullialdus	−22.3	−19.8	OPX	high	enhanced in central peak
Oriente	−94.5	−17.6	An	high	inner and outer basin rings
Korolev	−156.5	−5.5	An, OPX	high	small craters on inner ring
Copernicus	−20.1	10	An, Ol	low	enhanced in central peak
Appennine Bench	−6.6	25.7	OPX	high	enhanced in px-bearing massifs
Montes Alpes	−2.2	47.7	OPX	—	enhanced in px-bearing massifs
Compton–Belkovich	100.5	60.9	silicic	high	enhanced on domes

of each of these types of features are presented in [figure 3](#) along with colour composites to show the mineral variability and relative band depth maps to show the spatial extent of the OH<sup>−</sup> signature. In the colour composite, anorthosite and silicic material appears as blue, orthopyroxene appears as cyan, clinopyroxene appears as yellow or orange, and olivine appears as pink or red. Hydroxyl signatures are found in association with several different lithologies; however, if olivine or pyroxene dominates a spectral signature, spectrally neutral minerals such as anorthosite are likely to still be present in the rocks and regolith mixtures. Given the spectral resolution of M<sup>3</sup> in the 2800 nm region, it is not possible to explicitly identify which of these minerals the OH<sup>−</sup> is bound to.

Compton–Belkovich is a silicic construct [40] associated with a localized thorium hotspot [21], located at about 61° N, 100° E in the lunar highlands. Although Compton–Belkovich is located at high latitude where adsorbed water is also present, the OH<sup>−</sup> relative band depth on the silicic dome itself is several standard deviations deeper than in the surrounding terrain ([figure 3g](#); electronic supplementary material, table S1). This anomaly was identified and described by Petro *et al.* [41] and later by Battacharya [42]. More recent work by Li & Milliken [43] has shown that this anomaly is still evident when using their revised thermal correction methodology.

Although more spatially diffuse, elevated OH<sup>−</sup> signatures are also present in several basin rings. Oriente Basin, located near 95° W and 18° S, offers perhaps the best example of this. As illustrated in [figure 3h](#), OH<sup>−</sup> enhancements are observed throughout the inner and outer basin rings, associated with anorthosite. Korolev Crater, also located in the highlands, exhibits a similar enrichment in OH<sup>−</sup> in its rings, although the rings are more degraded and the OH<sup>−</sup> signature is strongest within smaller craters that have impacted ring material. Similarly, Chaffee S Crater, which impacted the inner ring of the Apollo Basin on the edge of the SPA, appears to have also exposed OH<sup>−</sup>-enriched material.

Materials excavated in the central peaks of both Bullialdus [44] and Copernicus Craters ([figure 3e,i](#)) exhibit enhanced OH<sup>−</sup>; however, many other central peaks of similarly sized craters, such as Aristillus or many craters within the SPA (electronic supplementary material, table S1), appear no different from their surroundings. Like Bullialdus, which impacted near the inner ring of Mare Nubium [44], Copernicus lies along a concentric ring centred on the Imbrium Basin, and may be re-excavating material brought closer to the surface by the larger impact. The OH<sup>−</sup> signature at Copernicus is associated with both anorthositic and olivine-bearing material ([figure 3e](#)).

A broken ring of massifs, including the Appennine Bench and the Montes Alpes, encircle the Imbrium Basin, and may represent basin ejecta or basin ring material [45]. Hydroxyl is found in association with orthopyroxene-bearing lithologies in many of these massifs. As illustrated in [figure 3](#), not all orthopyroxene-rich material (cyan in [figure 3f](#)) is necessarily associated with enhanced OH<sup>−</sup> ([figure 3j](#)). However, those with the most pristine orthopyroxene signatures are typically also OH<sup>−</sup> rich.

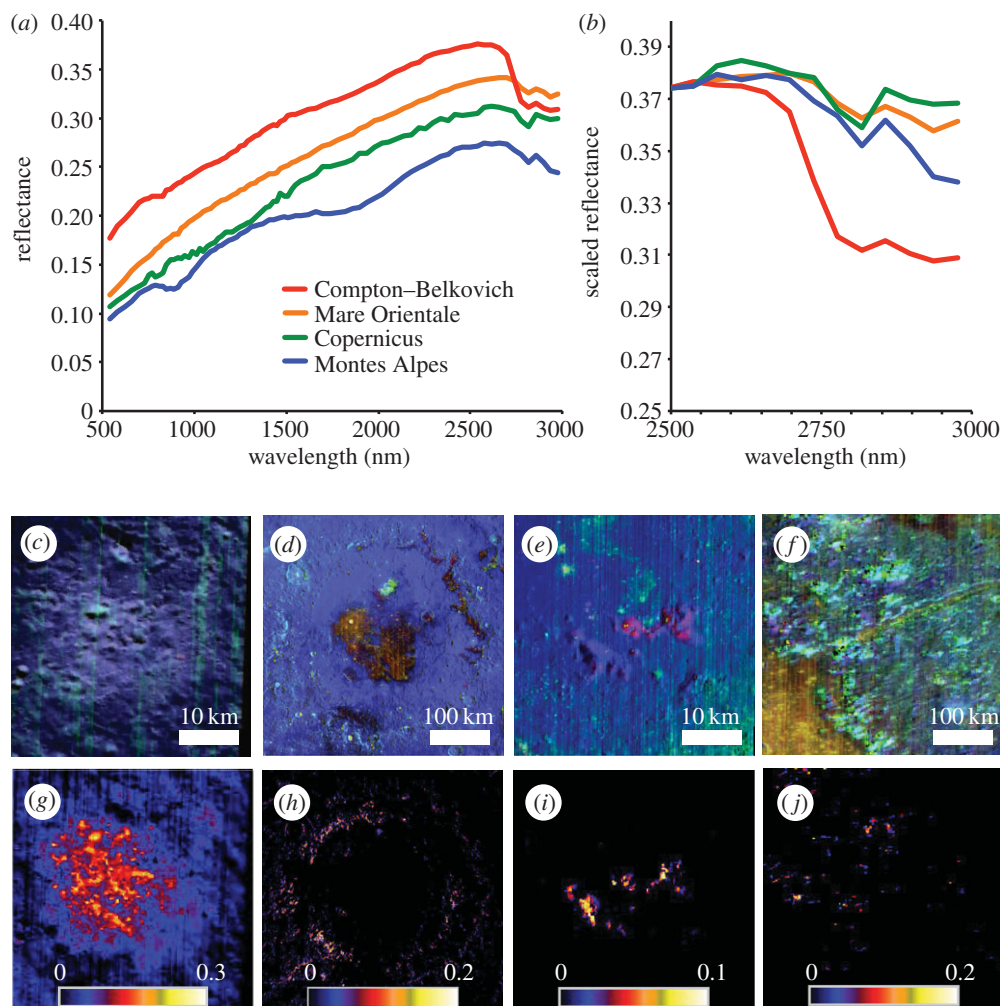


**Figure 3.** Spectral signature (*a,b*) and geographical distribution (*c–j*) at an example of a silicic construct, Compton–Belkovich (*c,g*); a ringed basin, Orientale (*d,h*); a central peak, Copernicus (*e,i*); and isolated massifs in the Montes Alpes (*f,j*). (*a*) Spectra for each site; (*b*) spectra normalized at 2500 nm (all sites scaled to the reflectance value for Compton–Belkovich) showing the relative strengths of the  $\text{OH}^-$  band at each site. (*c–f*) RGB composite images of each site: red, integrated 1000 nm band depth; green, integrated 2000 nm band depth; and blue, reflectance at 1500 nm. (*g–j*) Colour ramp images of  $\text{OH}^-$  relative band depth.

## 4. Discussion

### (a) Hydroxylation of material sourced at depth

Many of the  $\text{OH}^-$  anomalies found across the Moon can be traced to materials exposed from depth by basin-scale impacts. The impacts that produced the Korolev (417 km diameter) and Orientale (937 km diameter) Basins penetrated deep (30 km+) into the primordial lunar highland crust, though they may not have reached the lunar mantle. By contrast, the impact that produced the Imbrium Basin is likely to have excavated mantle material. Unlike Korolev and Orientale, the hydroxylated material associated with Imbrium is also associated with olivine or orthopyroxene, both of which are likely to be found in the lunar mantle. However, subsequent intrusive and extrusive volcanism in the PKT also delivered olivine and orthopyroxene to the lunar nearside, making the provenance of those minerals around Imbrium disputable.



Excavated  $\text{OH}^-$ -enriched materials are sometimes associated with thorium enhancements, potentially suggesting an association with KREEP material. Both Korolev and Orientale are reported as minor regional thorium highs [21]. However, within the PKT, where the strongest regional thorium enhancement occurs, many thorium highs are not associated with  $\text{OH}^-$ . In some cases, such as Copernicus Crater, the  $\text{OH}^-$  signature corresponds to a thorium low. This suggests that, at least in the PKT, there is not a clear direct relationship between KREEP and  $\text{OH}^-$ , probably due to the complicated volcanic history of the region and the different sensing depths of near-infrared and gamma-ray spectroscopy.

The SPA Basin is the largest impact basin on the Moon, and should have excavated significant amounts of lower crust and mantle material. However, few craters within SPA exhibit  $\text{OH}^-$  relative band depths in excess of the local global mean; in fact, most are depleted in  $\text{OH}^-$  relative to the global mean. One exception to this is within the Apollo Basin, which was formed near the northern edge of the basin. The mafic anomaly in SPA is dominated by the spectral signature of orthopyroxene, with some clinopyroxene concentrated in the centre near Mafic Mound [46]. It is possible that, following the SPA-forming impact, a large melt sheet filled much of the centre of the basin, which would have retained enough heat on cooling to differentiate (e.g. [47,48]), potentially also leading to the loss of volatiles. Petro *et al.* [49] investigated the composition of the Apollo Basin and suggested that, probably due to its positioning near the edge of SPA, the impact that formed Apollo may have excavated through the melt sheet, and into the unmelted, uplifted lower crustal material.

Taken together, these observations suggest that the base of the lunar crust may originally have been hydrated. Basins such as Korolev and Orientale, which impacted into thick anorthositic crust, may have approached this lower hydrated layer. In the PKT, however, extensive bombardment and thinning of the lithosphere may have allowed more degassing and dehydration of the lower crust [50]. This may explain why lower crustal samples returned from the lunar nearside that are high in KREEP are not generally enriched in  $\text{OH}^-$ .

## (b) Hydroxylation of extrusive lithologies

Silicic domes, such as those at Compton–Belkovich, have been interpreted as volcanic constructs consisting of highly silicic magmas, formed through either silicate liquid immiscibility or basaltic underplating [51]. The most  $\text{OH}^-$ -enriched portions of Compton–Belkovich are associated with small, blocky domes, probably representing the last volcanic products produced in the complex [40]. As relatively late-staged volcanic features, melting was probably caused by the heat-producing elements associated with KREEP. The association of  $\text{OH}^-$  with silicic domes appears consistent with  $\text{OH}^-$  concentrating along with urKREEP in the last liquids of the magma ocean. However, if the silicic magma was created by basaltic underplating of the anorthositic crust, it is also possible that  $\text{OH}^-$ , sequestered in the lower crust, could have concentrated in the silicic melts before eruption.

Studies conducted using a new method for thermal removal have revealed  $\text{OH}^-$  in association with many of the lunar pyroclastic deposits [37,38]. This is consistent with sample studies that suggest that pyroclastic deposits originated in a water-bearing mantle source [4]. Using the initial thermally corrected level 2  $\text{M}^3$  data, pyroclastic deposits do not appear to exhibit an  $\text{OH}^-$  anomaly relative to their surroundings. However, as described previously, this is potentially because thermal emission is muting any  $\text{OH}^-$  relative band depth at long wavelengths. Unfortunately, this means that any search for  $\text{OH}^-$  anomalies in the mare regions using  $\text{M}^3$  data will be strongly dependent on the thermal modelling and spectral calibration.

## 5. Conclusion

The distribution of  $\text{OH}^-$  on and in the Moon provides important constraints on our understanding of the formation of the Moon, evolution of the terrestrial planets and current surface processing of airless bodies. Although the large-scale regional spectral signature of  $\text{OH}^-$

observed on the Moon is probably due to relatively recent processes associated with solar wind, small, localized  $\text{OH}^-$  anomalies may provide a glimpse into the internal hydration state of the Moon. These  $\text{OH}^-$  anomalies are observed across the Moon, associated with specific geological features. Many anomalies are associated with large (more than 300 km diameter) impact basins that would have probably excavated material from the lower crust or upper mantle. Others are related to silicic constructs, formed by highly evolved magmatism. The relationship between  $\text{OH}^-$  anomalies and KREEP (by proxy of thorium content) suggests that, on the whole, strong anomalies are generally more common in KREEP-rich terrain, though many KREEP-rich regions, particularly in the PKT, are quite low in  $\text{OH}^-$ . If some  $\text{OH}^-$  was concentrated in nominally anhydrous lower crust and/or upper mantle during magma ocean formation, it may be decoupled from the KREEP signature. However, silicic constructs, if formed by underplating and melting of the lower crust by KREEP-rich basalt, could potentially assimilate both  $\text{OH}^-$  and KREEP.

**Data accessibility.** M<sup>3</sup> level 2 data can be accessed through the Planetary Data System, Imaging Node (<http://pds-imaging.jpl.nasa.gov/volumes/m3.html>). In addition to the data, a tutorial for working with the data is included at that web address. The formal description of the archive (SIS document) can be accessed directly at [http://pds-imaging.jpl.nasa.gov/data/m3/CH1M3\\_0001/DOCUMENT/ARCHSIS.PDF](http://pds-imaging.jpl.nasa.gov/data/m3/CH1M3_0001/DOCUMENT/ARCHSIS.PDF).

**Authors' contributions.** R.L.K. conducted spectral parameter mapping, led spectral analysis and interpretation and wrote the first draft of the manuscript. N.E.P. conducted critical geological analysis, particularly of the Compton–Belkovich silicic complex and the Apollo Basin. He also assisted with data interpretation, revisions of the initial draft, and final approval of the submitted version.

**Competing interests.** We have no competing interests.

**Funding.** R.L.K. was supported by the NASA SSERVI grant to JHU/APL. N.E.P. was supported by NASA and the Lunar Reconnaissance Orbiter Mission.

## References

1. Wood JA, Dickey Jr JS, Marvin UB, Powell BN. 1970 Lunar anorthosites and a geophysical model for the Moon. In *Proc. of the Apollo 11 Lunar Science Conference, Houston, TX, 5–8 January 1970*, pp. 965–988. New York, NY: Pergamon Press.
2. Warren PH. 1985 The magma ocean concept and lunar evolution. *Annu. Rev. Earth Planet. Sci.* **13**, 201–240. (doi:10.1146/annurev.ea.13.050185.001221)
3. Hess PC, Parmentier EM. 1995 A model for the thermal and chemical evolution of the Moon's interior: implications for the onset of mare volcanism. *Earth Planet. Sci. Lett.* **134**, 501–514. (doi:10.1016/0012-821X(95)00138-3)
4. Saal AE, Hauri EH, Lo Cascio M, Van Orman JA, Rutherford MC, Cooper RF. 2008 Volatile content of lunar volcanic glasses and the presence of water in the Moon's interior. *Nature* **454**, 192–196. (doi:10.1038/nature07047)
5. Hauri EH, Weinreich T, Saal AE, Rutherford MC, Van Orman JA. 2011 High pre-eruptive water contents preserved in lunar melt inclusions. *Science* **333**, 213–215. (doi:10.1126/science.1204626)
6. McCubbin FM, Steele A, Hauri EH, Nekvasil H, Yamashita S, Hemley R. 2010 Nominally hydrous magmatism on the Moon. *Proc. Natl Acad. Sci. USA* **27**, 11 223–11 228. (doi:10.1073/pnas.1006677107)
7. Boyce JW, Liu Y, Rossman GR, Guan Y, Eiler JM, Stolper EM, Taylor LA. 2010 Lunar apatite with terrestrial volatile abundances. *Nature* **466**, 466–469. (doi:10.1038/nature09274)
8. Barnes JJ, Franchi IA, Anand M, Tartèse R, Starkey NA, Koike M, Sano Y, Russell SS. 2013 Accurate and precise measurements of the D/H ratio and hydroxyl content in lunar apatites using NanoSIMS. *Chem. Geol.* **337–338**, 48–55. (doi:10.1016/j.chemgeo.2012.11.015)
9. Anand M. 2010 Lunar water: a brief review. *Earth Moon Planets* **107**, 65–73. (doi:10.1007/s11038-010-9377-9)
10. Anand M, Tartèse R, Barnes JJ. 2014 Understanding the origin and evolution of water in the Moon through lunar sample studies. *Phil. Trans. R. Soc. A* **372**, 20130254. (doi:10.1098/rsta.2013.0254)
11. McCubbin FM *et al.* 2015 Magmatic volatiles (H, C, N, F, S, Cl) in the lunar mantle, crust, and regolith: abundances, distributions, processes, and reservoirs. *Am. Mineral.* **100**, 1668–1707. (doi:10.2138/am-2015-4934CCBYNCND)

12. McCubbin FM, Jolliff BJ, Nekvasil H, Carpenter PK, Zeigler RA, Steele A, Elardo SM, Lindsley DH. 2011 Fluorine and chlorine abundances in lunar apatite: implications for heterogeneous distributions of magmatic volatiles in the lunar interior. *Geochim. Cosmochim. Acta* **75**, 5073–5093. (doi:10.1016/j.gca.2011.06.017)
13. Tartèse R, Anand M, McCubbin FM, Elardo SM, Shearer Jr CK, Franchi IA. 2014 Apatites in lunar KREEP basalts: the missing link to understanding the H isotope systematics of the Moon. *Geology* **42**, 363–366. (doi:10.1130/G35288.1)
14. Goswami JN, Annadurai M. 2009 Chandrayaan-1: India's first planetary science mission to the Moon. In *Proc. 40th Lunar and Planetary Science Conference, The Woodlands, TX, 23–27 March 2009*, abstract 2571. See <http://www.lpi.usra.edu/meetings/lpsc2009/pdf/2571.pdf>.
15. Pieters CM *et al.* 2009 Character and spatial distribution of OH/H<sub>2</sub>O on the surface of the Moon seen by M3 on Chandrayaan-1. *Science* **326**, 568–572. (doi:10.1126/science.1178658)
16. Sunshine JM, Farnham TL, Feaga LM, Groussin O, Merlin F, Milliken RE, A'Hearn MF. 2009 Temporal and spatial variability of lunar hydration as observed by the Deep Impact spacecraft. *Science* **326**, 565–568. (doi:10.1126/science.1179788)
17. Clark RN. 2009 Detection of adsorbed water and hydroxyl on the Moon. *Science* **326**, 562–564. (doi:10.1126/science.1178105)
18. McCord TB, Taylor LA, Combe J-P, Kramer G, Pieters CM, Sunshine JM, Clark RN. 2011 Sources and physical processes responsible for the OH/H<sub>2</sub>O in the lunar soil as revealed by the Moon Mineralogy Mapper (M3). *J. Geophys. Res.* **116**, E00G05. (doi:10.1029/2010JE003711)
19. Wieczorek MA, Phillips RJ. 2000 The 'Procellarum KREEP Terrane': implications for mare volcanism and lunar evolution. *J. Geophys. Res.* **105**, 20 417–20 430. (doi:10.1029/1999JE001092)
20. Warren PH. 2003 The Moon. In *Treatise on geochemistry*, vol. 1 (eds H Holand, K Turekian), pp. 559–599. New York, NY: Elsevier.
21. Lawrence DJ, Elphic RC, Feldman WC, Prettyman TH, Gasnault O, Maurice S. 2003 Small-area thorium features on the lunar surface. *J. Geophys. Res.* **108**, JE002050. (doi:10.1029/2003JE002050)
22. Green RO *et al.* 2011 The Moon Mineralogy Mapper (M3) imaging spectrometer for lunar science: instrument description, calibration, on-orbit measurements, science data calibration and on-orbit validation. *J. Geophys. Res.* **116**, E00G19. (doi:10.1029/2011JE003797)
23. Boardman JW *et al.* 2011 Measuring moonlight: an overview of the spatial properties, lunar coverage, selenolocation, and related level 1B products of the Moon Mineralogy Mapper. *J. Geophys. Res.* **116**, E00G14. (doi:10.1029/2010JE003730)
24. Clark RN, Pieters CM, Green RO, Boardman JW, Petro NE. 2011 Thermal removal from near-infrared imaging spectroscopy data of the Moon. *J. Geophys. Res.* **116**, E00G16. (doi:10.1029/2010JE003751)
25. Besse S *et al.* 2013 A visible and near-infrared photometric correction for Moon Mineralogy Mapper (M3). *Icarus* **222**, 229–242. (doi:10.1016/j.icarus.2012.10.036)
26. Libowitzky E, Rossman G. 1997 An IR absorption calibration for water in minerals. *Am. Mineral.* **82**, 1111–1115. (doi:10.2138/am-1997-11-1208)
27. Milliken RE, Mustard JF. 2005 Quantifying absolute water content of minerals using near-infrared reflectance spectroscopy. *J. Geophys. Res.* **110**, E12001. (doi:10.1029/2005JE002534)
28. Milliken RE, Mustard JF. 2007 Estimating the water content of hydrated minerals using reflectance spectroscopy. I. Effects of darkening agents and low-albedo materials. *Icarus* **189**, 550–573. (doi:10.1016/j.icarus.2007.02.017)
29. Milliken RE, Mustard JF. 2007 Estimating the water content of hydrated minerals using reflectance spectroscopy. II. Effects of particle size. *Icarus* **189**, 574–588. (doi:10.1016/j.icarus.2006.12.028)
30. Hapke BW. 1993 *Theory of reflectance and emittance spectroscopy*. Cambridge, UK: Cambridge University Press.
31. Li S, Milliken RE. 2016 An empirical thermal correction for Moon Mineralogy Mapper data constrained by laboratory spectra and Diviner temperatures. *J. Geophys. Res.* **121**, 2081–2107. (doi:10.1002/2016JE005035)
32. Vasavada AR, Bandfield JL, Greenhagen BT, Hayne PO, Siegler MA, Williams J-P, Paige DA. 2012 Lunar equatorial surface temperatures and regolith properties from the Diviner Lunar Radiometer Experiment. *J. Geophys. Res.* **117**, E00H18. (doi:10.1029/2011JE003987)

33. Bandfield JL, Edwards CS, Poston MJ, Klima RL. 2016 Lunar H<sub>2</sub>O/OH<sup>-</sup> distributions: revised infrared spectra from improved thermal corrections. In *Proc. 47th Lunar and Planetary Science Conference, The Woodlands, TX, 21–25 March 2016*, abstract 1594. See <http://www.hou.usra.edu/meetings/lpsc2016/pdf/1594.pdf>.
34. Cheek LC *et al.* 2011 Goldschmidt crater and the Moon's north polar region: results from the Moon Mineralogy Mapper (M3). *J. Geophys. Res.* **116**, E00G02. (doi:10.1029/2010JE003702)
35. Hibbitts CA, Grieves GA, Poston MJ, Dyar MD, Alexandrov AB, Johnson MA, Orlando TM. 2011 Thermal stability of water and hydroxyl on the surface of the Moon from temperature-programmed desorption measurements of lunar analog materials. *Icarus* **213**, 64–72. (doi:10.1016/j.icarus.2011.02.015)
36. Poston MJ, Grieves GA, Aleksandrov AB, Hibbitts CA, Dyar MD, Orlando TM. 2013 Water interactions with micronized lunar surrogates JSC-1A and albite under ultra-high vacuum with application to lunar observations. *J. Geophys. Res.* **118**, 105–115. (doi:10.1029/2012JE004283)
37. Li S, Milliken RE. 2014 Quantitative mapping of hydration in lunar pyroclastic deposits: insights into water from the lunar interior. In *Proc. 45th Lunar and Planetary Science Conference, The Woodlands, TX, 17–21 March 2014*, abstract 2012. See <http://www.hou.usra.edu/meetings/lpsc2014/pdf/2012.pdf>.
38. Li S, Milliken RE. 2015 Water in lunar pyroclastic deposits: linking orbital observations to interior processes. In *Proc. 46th Lunar and Planetary Science Conference, The Woodlands, TX, 16–20 March 2015*, abstract 1224. See <http://www.hou.usra.edu/meetings/lpsc2015/pdf/1224.pdf>.
39. Klima RL *et al.* 2011 New insights into lunar petrology: distribution and composition of prominent low-Ca pyroxene exposures as observed by the Moon Mineralogy Mapper (M3). *J. Geophys. Res.* **116**, E00G06. (doi:10.1029/2010JE003719)
40. Jolliff BL *et al.* 2011 Non-mare silicic volcanism on the lunar farside at Compton-Belkovich. *Nat. Geosci.* **4**, 566–571. (doi:10.1038/NGEO1212)
41. Petro NE, Isaacson PJ, Pieters CM, Jolliff BL, Carter LM, Klima RL. 2013 Presence of H<sub>2</sub>O/OH associated with the lunar Compton-Belkovich volcanic complex identified by the Moon Mineralogy Mapper (M3) data. In *Proc. 44th Lunar and Planetary Science Conference, The Woodlands, TX, 18–22 March 2013*, abstract 2688.
42. Bhattacharya S, Saran S, Dagar A, Chauhan P, Chauhan M, Kumar AASK. 2013 Endogenic water on the Moon associated with nonmare silicic volcanism: implications for hydrated lunar interior. *Curr. Sci.* **105**, 685–691.
43. Li S, Milliken RE. 2016 Heterogeneous water content in the lunar interior: insights from orbital detection of water in pyroclastic deposits and silicic domes. In *Proc. 47th Lunar and Planetary Science Conference, The Woodlands, TX, 21–25 March 2016*, abstract 1568. See <http://www.hou.usra.edu/meetings/lpsc2016/pdf/1568.pdf>.
44. Klima R, Cahill J, Hagerty J, Lawrence D. 2013 Remote detection of magmatic water in Bullialdus Crater on the Moon. *Nat. Geosci.* **6**, 737–741. (doi:10.1038/ngeo1909)
45. Spudis PD, Hawke BR, Lucey PG. 1988 Materials and formation of the Imbrium basin. *Lunar Planet. Sci.* **18**, 155–168.
46. Moriarty DP, Pieters CM. 2015 The nature and origin of Mafic Mound in the South Pole-Aitken Basin. *Geophys. Res. Lett.* **42**, 7907–7915. (doi:10.1002/2015GL065718)
47. Pieters CM, Tompkins S, Head JW, Hess PC. 1997 Mineralogy of the mafic anomaly in the South Pole-Aitken Basin: implications for excavation of the lunar mantle. *Geophys. Res. Lett.* **24**, 1903–1906. (doi:10.1029/97GL01718)
48. Hurwitz DM, Kring DA. 2014 Differentiation of the South Pole-Aitken basin impact melt sheet: implications for lunar exploration. *J. Geophys. Res.* **119**, 1110–1133. (doi:10.1002/2013JE004530)
49. Petro NE *et al.* 2011 Lower crustal materials exposed in the Apollo Basin revealed using Moon Mineralogy Mapper (M3) data. In *Proc. 41st Lunar and Planetary Science Conference, The Woodlands, TX, 1–5 March 2010*, abstract 1802. See <http://www.lpi.usra.edu/meetings/lpsc2010/pdf/1802.pdf>.
50. Barnes JJ, Tartèse R, Anand M, McCubbin FM, Neal CR, Franchi IA. 2016 Early degassing of lunar urKREEP by crust-breaching impact(s). *Earth Planet. Sci. Lett.* **447**, 84–94. (doi:10.1016/j.epsl.2016.04.036)
51. Glotch TD *et al.* 2010 Highly silicic compositions on the Moon. *Science* **329**, 1510–1513. (doi:10.1126/science.1192148)